Mechano-synthesis and degradation of an equimolar Li-Sn alloy

Sara Sofia dos Santos Elias sara.elias@tecnico.ulisboa.pt

Instituto Superior Técnico, Lisbon, Portugal
May 2022

A B S T R A C T

Lithium-Tin (Li-Sn) alloys are an attractive solution for plasma facing components of nuclear fusion reactors and have received considerable attention regarding lithium-ion batteries. Mechano-synthesis, via high energy milling, has been demonstrated to be an effective method to produce prototype Li-Sn alloys. However, due to the large number of parameters involved in this processing route, their effects on the final microstructure and composition of the alloys remain relatively understudied. The description and understanding of the reaction path remain rather incomplete. In this work, the impact of the milling rate (150 rpm and 500 rpm) and milling ball diameter (6 mm, 10 mm, and 15 mm) on the final microstructure of an equimolar Li-Sn alloy is studied. Milling times from 0.5 h to 64 h are tested. The resultant phase composition was assessed in detail by a combination of ion beam analysis, X-ray diffraction, differential scanning calorimetry, and gravimetric analysis. Milling rate is the milling parameter presenting the major effect on reaction kinetics. Milling experiments at 500 rpm, using 10 mm balls, presented the highest milling efficiency (milling mass yield, y_M ~ 86%), and resulted in the most homogeneous equimolar alloy, with LiSn as the major phase. Mechano-synthesis progresses in two fronts: Li-rich Li-Sn intermetallics preferentially form at the surface of the initial (Li) cuts, whereas Sn-rich Li-Sn intermetallics preferentially form at the surface of the original β-Sn powders. These two fronts converge, at a later stage, to a base LiSn composition, with Li_2Sn_5 and possibly with small crystallite size Li-rich Li-Sn intermetallics.

Keywords: Li-Sn alloys; Mechano-synthesis; Oxidation; X-ray Diffraction.

1. Introduction

Lithium-Tin (Li-Sn) alloys, which have received considerable attention regarding lithium-ion batteries in the past few decades [1], have recently been identified as an attractive solution for plasma facing components of nuclear fusion reactors [2].

Production of these alloys, however, faces some challenges: the chemical reactivity of Li, which must be mitigated, requiring special conditions during processing to avoid sample contamination, and the formation of stable high melting temperature Li-rich Li-Sn intermetallics, which must be prevented. Mechano-synthesis (MS), via high energy milling, is an alternative method to casting [3–11] to produce tailored Li-Sn alloys. MS has been demonstrated to be an effective technique for production of Li-Sn alloys with Li content up to 50 at. % [12–16]. The large number of parameters involved in this processing route has stalled the study of their effects on the final microstructure and composition, which remains relatively understudied. The description and understanding of the reaction path during mechano-synthesis remains rather incomplete.

This work aims to study the impact of the milling rate and milling ball diameter on the final microstructure and composition of an equimolar Li-Sn alloy (50Li-Sn) and identify the milling parameters that result in both the highest milling mass yield and the most homogenous equimolar Li-Sn alloy. The feasibility of X-ray diffraction use to characterize the alloys produced is also assessed.

2. Mechano-synthesis of Li-Sn alloys

The first studies reporting the use of mechano-synthesis to produce Li-Sn intermetallics were carried out in the field of Li-ion batteries. They mainly focused on the characterization of the electrochemical properties of Li-rich intermetallics [17–19], and heat capacity calculations for improving the thermodynamic description of the Li-Sn system in the Li-rich part of the phase diagram [7]. Two studies reported the mechano-synthesis of LiSn and Li_2Sn_5 using a vibratory mill, for 48 h of milling time, with subsequent 7 day annealing treatment [18,19]. Comprehensive phase characterization of the MS output, however, was not carried out and no description of the mechano-synthesis process, nor of the alloying mechanisms was presented.

Recently, Li-Sn alloys, in particular with low Li content (< 25 at. % [16]), have received considerable attention for application in plasma facing components of nuclear fusion reactors [12–16]. Costa *et al.* [14] reported the successful production of Li-Sn alloys with Li compositions in the 5-25 Li (at. %) interval through mechano-synthesis.

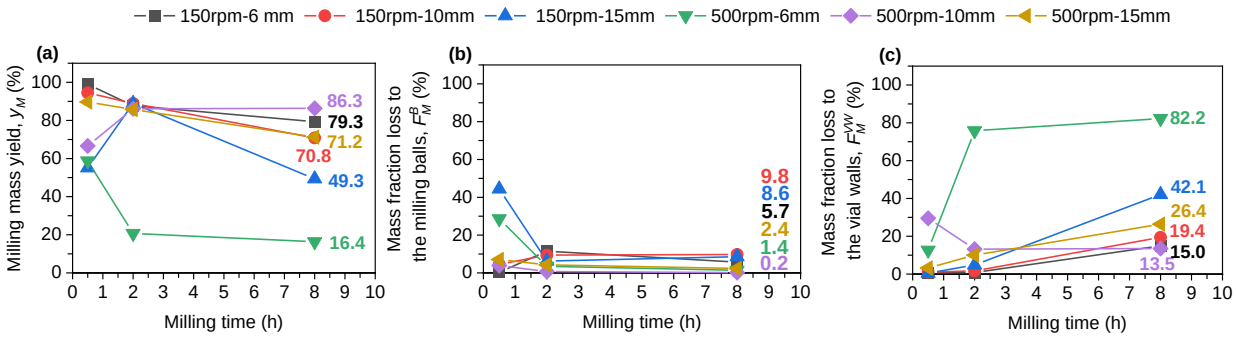

Figure 1 - Milling mass yield evolution with milling time: (a) milling mass yield, y_M, (b) mass fraction loss to the milling balls, F_{mass}^{B}, and (c) mass fraction loss to the vial walls, F_{mass}^{VW}.

Formation of both equilibrium and out of equilibrium crystalline intermetallics was observed. 25Li-Sn (at. %) alloy milled for 12 h presented β-Sn, Li_2Sn_5 and LiSn. Post-annealing at 160º for 2 h promoted growth of the stable Li_2Sn_5 intermetallic, with a correspondent partial decrease of the fraction of LiSn. Nevertheless, the predominant cold-welding behaviour of these alloys when mechanically milled results in low milling mass yields (< 20 % [16]). The higher the β-Sn content, the lower the milling mass yield. Moreover, due to the low density of Li compared to Sn, preparation of alloys with Li content below 5 at. %, is difficult. Mateus *et al.* [13] developed a lithium dilution method for the production of Li-Sn alloys with Li content below 5 at. %. They prepared a 50 Li-Sn (at. %) master powder alloy and then achieved the desired 5Li-Sn (at. %) and 1Li-Sn (at. %) alloys by dilution of the master powders with the correspondent amounts of pure Sn. Although compositional analysis confirmed that the desired Li:Sn stoichiometry was attained, phase characterization of the master alloy revealed the presence of β-Sn, Li_2Sn_5, and LiSn, even after annealing treatment at 160 ºC for 2 h. Therefore, improvement of the mechano-synthesis process and respective phase analysis is still necessary and a comprehensive study of the reaction path and influence of the milling parameters on the final microstructure and composition of Li-Sn alloys is lacking.

3. Experimental Procedure

3.1. Materials

Small pieces of Li metal (99 at. %, ~2mm, Sigma-Aldrich) and Sn atomised powders (99.9 wt. %, < 45 µm, Makin Metal Powders (UK) Ltd) were used as starting materials.

3.2. 50Li-Sn alloy production

Two milling rates (150 rpm and 500 rpm), three milling ball diameters (6 mm, 10 mm, and 15 mm), and

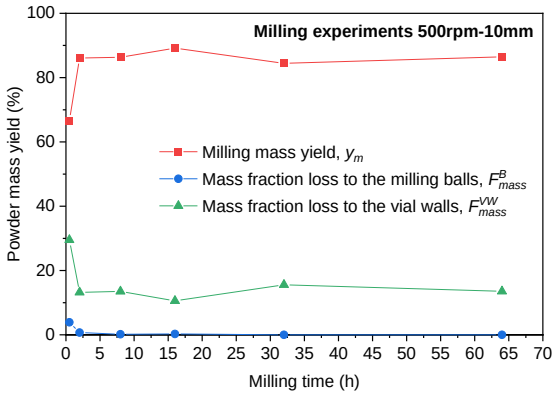

Figure 2 - Powder mass yield evolution with milling time for milling experiments with 500rpm-10mm, run for 0.5 h, 2 h, 8 h, 16 h, 32 h and 64 h.

milling times from 0.5 h to 64 h were tested to produce the equimolar alloy. The following milling condition base acronym is adopted, e.g.: 500rpm-10mm, meaning 500 rpm, and 10 mm diameter milling balls. When referring to a particular effective milling time, for a certain milling condition, the effective milling time is added to the milling condition base acronym, e.g.: 500rpm-10mm-8h. A 10:1 ball-to-powder ratio was used. The mass of the powder milling batch was set to 3 g, meaning 34 spheres of 6 mm, 7 spheres of 10 mm, and 2 spheres of 15 mm were used, all made of AISI 420C steel. Experiments were conducted on a Retsch PM100 planetary ball mill using a AISI 420C steel 50mL vial. All milling cycles were carried out with 10 min uninterrupted milling followed by a 5 min stopping interval to allow the milling media and milled batch to cool, avoiding overheating. To prevent powder contamination from atmospheric gases, starting and processed materials storage, vial loading, sealing, opening, and sample handling was carried out under argon atmosphere (< 0.1 ppm H_2O/O_2), inside a glovebox (MBraun Unilab Plus). To seal the vial atmosphere during milling, a security hatch was used. Samples were carried to the characterization facilities inside small HDPE flasks sealed with an O-ring.

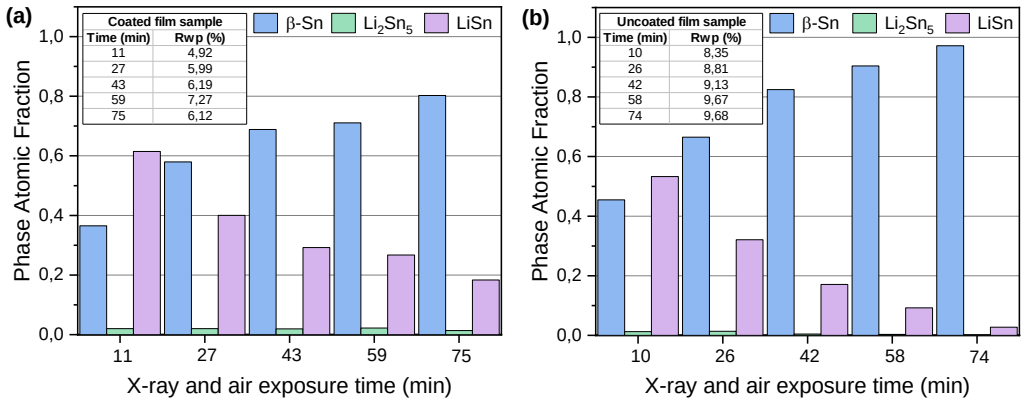

Figure 3 - Rietveld refinement results. Phase atomic fraction evolution with X-ray and air exposure time for: (a) coated film sample, and (b) uncoated film sample. All 500rpm-10mm-8h samples.

3.3. Characterization

Milled powders and milling balls were weighted after each milling cycle in order to characterize the process efficiency.

Ion Beam Analysis (IBA) was carried out in the 2.5 MeV Van de Graaff accelerator of CTN/IST.

XRD characterization was performed with a Bruker D8 ADVANCE Powder Diffractometer, using Cu-K_α radiation (electric potential difference of 40 kV, and electric current of 30 mA). The diffractograms were obtained with a step of 0.04º and acquisition time of 0.8 seconds. Two powder sample preparation methods were used, depending on the powder particle size after milling, assessed by visual inspection: powder film sample (particle size < 1 mm) or powder pellet sample (particle size > 1 mm). For certain milling time conditions, both powders and disc-like particles composed the mechano-synthesis product. Powders, as well as disc-like particles, were characterized using XRD. Either powders, disc-like particles, or pellets were put inside a small flask, two to three drops of liquid paraffin were added and then the flask was closed, sealed with an O-ring. Disc-like particles were treated as powders samples. Additional XRD simulations were carried out on GSAS-II software.

DSC thermal analysis was performed with a DSC 200 F3 Maia, from NETZSCH Premier Technologies, in the 150-250 ºC temperature range, with heating ramps of 10ºC/min, under N_2 atmosphere (50mL/min).

GA analysis was carried out in Setsys Evo 16 equipment, from Setaram, under air atmosphere. A gas flow of 30mL/min was used, and temperature was kept constant at 22 ºC.

4. Results and Discussion

4.1. Milling mass yield evolution with time

Milling efficiency of 50Sn-Li alloy has revealed to be considerable larger than of Li-Sn alloys with Li content below 25 at.% (< 20 % [16]). Overall, all milling experiments present milling mass yields above 40 %, expect for 500rpm-6mm (Figure 1). As milling progresses, loss of process efficiency is observed due to material adhesion and cold-welding to the milling media. The main source of material loss is powder adhesion and cold-welding to the vial walls with a general increasing tendency with milling time. Adhesion, and cold-welding to the milling balls, accounts for less than 10% of the total mass loss.

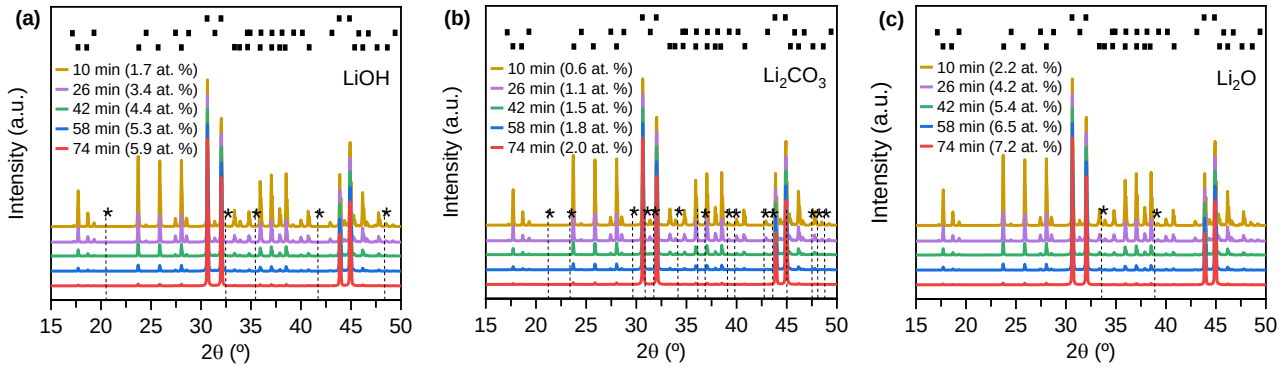

Figure 4 - Simulated diffractograms from uncoated film sample during X-ray and air exposure for 10 min, 26 min, 42 min, 58 min and 74 min, considering that mass gain observed in GA analysis is due to formation of: (a) LiOH, (b) Li_2CO_3, and (c) Li_2O. The patterns of β-Sn (first row), Li_2Sn_5 (second row), LiSn (third row), and of the tested Li-air reaction products (dashed line plus *) are shown. In brackets, respective Li-air reaction products atomic fraction (at. %), for each exposure time. Sample 500rpm-10mm-8h.

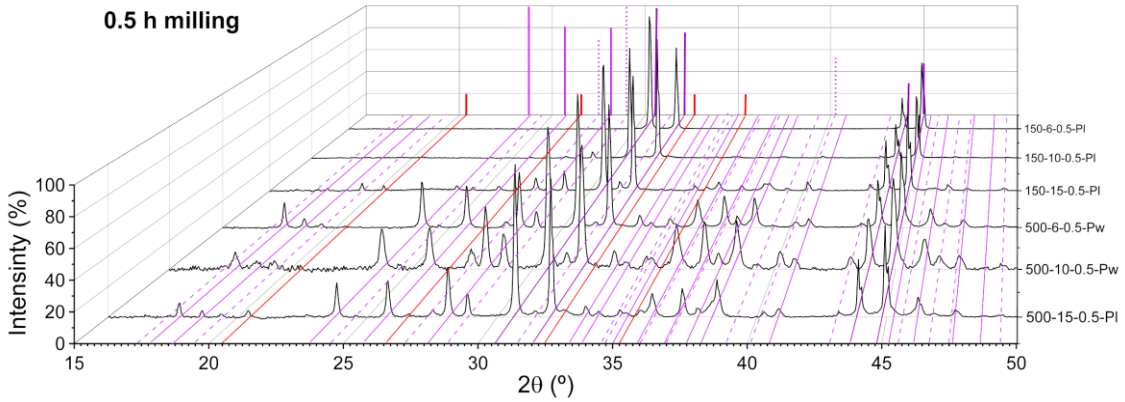

Figure 5 - XRD diffractograms of 50Li-Sn powders (Pw) and pellet (Pl) samples milled for 0.5 h. Phase pattern code: β-Sn (solid purple), Li_2Sn_5 (dash pink), LiSn (solid pink), and unidentified peaks peaks (solid red).

500rpm-10mm milling experiment series were further explored, with milling times up to 64 h being tested (Figure 2). A stationary y_M~86% was observed, indicating that balance is achieved between the kinetics of the mechanisms of adhesion and cold welding, on one hand, and de-adhesion and fracture, on the other hand.

4.2. Preliminary XRD Context Study: 50Li-Sn alloy chemical reactivity in air environment

A preliminary XRD Context Study was conducted, which allowed to identify vulnerabilities in 50Li-Sn alloy characterization via XRD, using liquid paraffin as a protective coating, when a portable controlled atmosphere sample stage is not available. From the equilibrium point of view, a 100 % LiSn phase composition is expected for a perfect equimolar Li-Sn alloy [20], after severe mechano-synthesis processing. In the starting stages of the mechano-synthesis process, mixtures with unreacted (Li) and β-Sn phases would be anticipated, which, as processing progresses, would evolve into mixtures of the LiSn phase with Li-rich and Sn-rich Li-Sn intermetallics. However, due to Li high diffusivity and chemical reactivity with atmospheric gases (O_2, N_2, H_2O, and CO_2), surface formation of Li-rich air reaction products (LiOH, Li_2CO_3, and Li_2O) inevitably occurs, compromising sample integrity. Five consecutive XRD runs were carried out on two coated and uncoated unexposed samples (with only ~2 min exposure to air, prior to XRD start, corresponding to sample preparation delay time). XRD tests were carried out on 500rpm-10mm-8h powder film samples.

XRD analysis, and following Rietveld Refinement of the obtained diffractograms, revealed that an induced radiation damage process of the protective liquid paraffin coating is observed due to X-ray exposure, with liquid paraffin exhibiting a decrease in its level of protective capability (Figure 3).

DSC complementary analysis of a 500rpm-10mm-8h sample, supported the XRD results, suggesting that LiSn and Li_2Sn_5, and eventually some Li-rich Li-Sn intermetallics, are the only phases present in the pristine milled powders, with no remnant of the β-Sn phase observed in XRD analysis (Figure 10b).

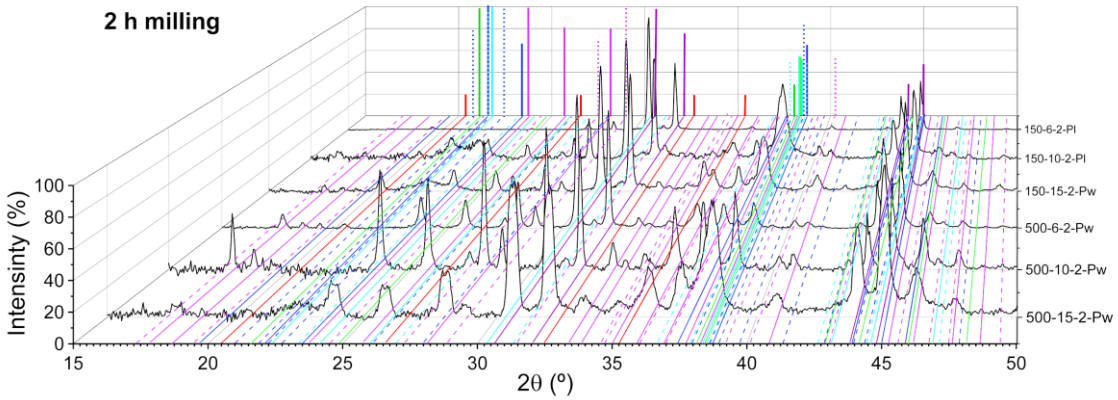

Figure 6 - XRD diffractograms of 50Li-Sn powders (Pw) and pellet (Pl) samples milled for 2 h. Phase pattern code: β-Sn (solid purple), Li_2Sn_5 (dash pink), LiSn (solid pink), Li_7Sn_3 (solid green), Li_5Sn_2 (dash light blue), $Li_{13}Sn_5$ (solid light blue), Li_7Sn_2 (dash dark blue), and $Li_{17}Sn_4$ (solid dark blue), and unidentified peaks peaks (solid red).

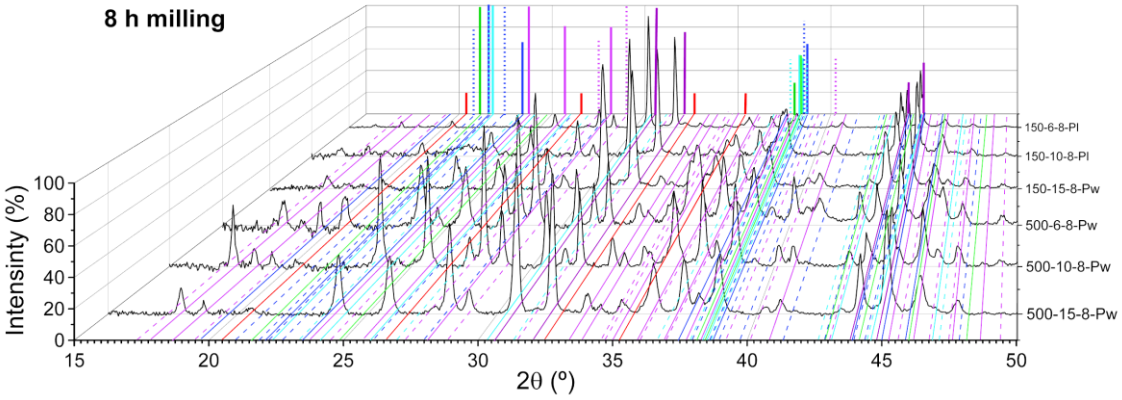

Figure 7 - XRD diffractograms of 50Li-Sn powders (Pw) and pellet (Pl) samples milled for 8 h. Phase pattern code: β-Sn (solid purple), Li_2Sn_5 (dash pink), LiSn (solid pink), Li_7Sn_3 (solid green), Li_5Sn_2 (dash light blue), $Li_{13}Sn_5$ (solid light blue), Li_7Sn_2 (dash dark blue), and $Li_{17}Sn_4$ (solid dark blue), and unidentified peaks peaks (solid red).

GA tests on two powder samples, coated and uncoated, allowed to confirm the role of X-rays in liquid paraffin loss of protection. While the coated sample suffers no mass change, the uncoated sample experiences a continuous mass change, with a 1.6% mass gain after 3 h exposed to air, at NTP conditions. GA complementary analysis also exposed the bias of XRD towards β-Sn phase. As can be observed in Figure 3, from 10 min to 26 min of X-ray and air exposure, LiSn atomic percentage decreases ~20 at. % (corresponding to ~10 Li at. % and ~10 β-Sn at. %). However, considering individual Li-air reaction product formation responsible for the observed GA mass gain, from 10 min to 26 min, LiOH formation only accounts for ~0.5 Li at. %, Li_2CO_3 for Li ~0.2 at. %, and Li_2O for Li ~1.3 at. %. Also, an unproportionally ~20 at. % increase of β-Sn is detected. It is proposed that, as degradation proceeds, Sn-enrichment in the vicinity of the metal-reaction layer interface reduces the X-rays beam depth of penetration (to 1.29 μm and to 1.55 μm, corresponding, respectively, to the θ incident angles of most intense LiSn and Li_2Sn_5 peaks) due to Sn high linear absorption coefficient [21]. As a result, LiSn and Li_2Sn_5 detectability decreases and XRD measurements become biased in favour of β-Sn phase.

Three additional XRD simulations of the uncoated film sample during X-ray and air exposure for 10 min, 26 min, 42 min, and 74 min, were carried out considering that mass gain observed in GA analysis is due to formation of LiOH, Li_2CO_3, and Li_2O, respectively (Figure 4). No characteristic peaks are observed, which together with GA results, demonstrate the incapacity of XRD technique to detect the formation of Li-air reaction products during 50Li-Sn degradation.

4.3. 50Li-Sn powder phase evolution

XRD and DSC analysis allowed to disclose the reaction path leading to the final alloy microstructure and composition. The formation of Li-rich Li-Sn intermetallics in the disc-like particles, derived from the initial Li pieces (Figure 8), is simultaneously accompanied by the formation of the Sn-rich Li_2Sn_5 intermetallic on the original β-Sn powders (Figure 5, and Figure 6). As milling progresses, both Li-rich and Sn-rich domains tend to evolve and transform towards

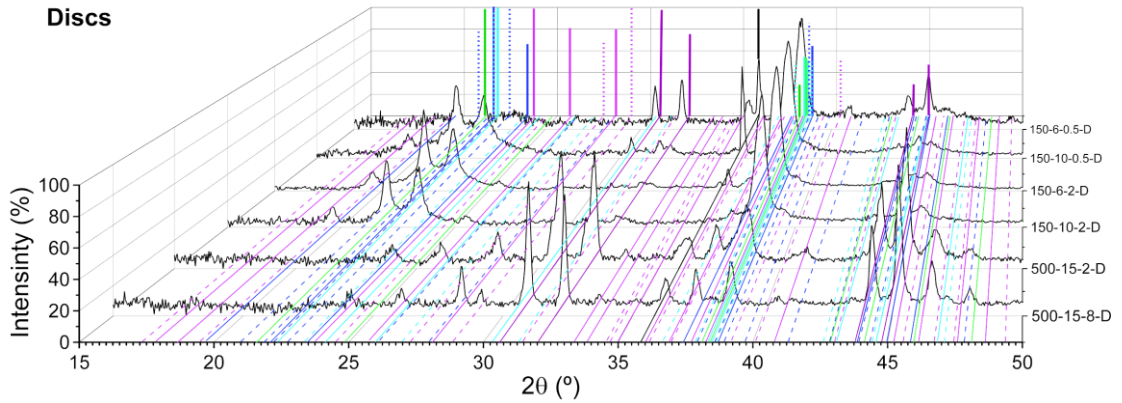

Figure 8 - XRD diffractograms of 50Li-Sn disc-like (D) samples. Phase pattern code: β-Sn (solid purple), Li_2Sn_5 (dash pink), LiSn (solid pink), Li_7Sn_3 (solid green), Li_5Sn_2 (dash light blue), $Li_{13}Sn_5$ (solid light blue), Li_7Sn_2 (dash dark blue), $Li_{17}Sn_4$ (solid dark blue), and (Li) (solid black).

the equilibrium phase LiSn (Figure 7). DSC analysis of 8 h milled samples confirmed that a final base LiSn composition, with Li_2Sn_5, and possibly with small crystallite size Li-rich Li-Sn intermetallics, is obtained. Precise identification of Li-rich Li-Sn intermetallics on XRD diffractograms proved to be difficult due to the crystallographic properties of these phases and the experimental constraints of XRD data acquisition. As these Li-Sn intermetallics have melting points, or are involved in invariant transformations, outside the tested DSC temperature range, DSC analysis was not able to clarify which phases are present. Additional XRD diffractograms simulations carried out attested the complexity and similarity of Li-rich Li-Sn intermetallics, and the XRD low sensitivity towards these phases (for crystallite sizes of 5 nm, simulations disclosed a ~15 wt.% detection limit).

4.3. Influence of milling parameters

Regarding the influence of the milling parameters on milling efficiency, the stochastic nature of the mechano-synthesis process, together with the fact that only one milling experiment for each milling time was carried out, do not allow to draw trustworthy conclusions. On the other hand, both DSC and XRD analysis allowed to conclude that milling rate is the milling parameter presenting the major effect on reaction kinetics, and hence on the final microstructure and composition of an equimolar Li-Sn alloy. The influence of milling ball diameter is not as pronounced. DRX analysis indicates a lower kinetics for milling experiments with 150 rpm, for which Li_2Sn_5 and LiSn peaks present lower intensity for all milling times, when compared to milling experiments with 500 rpm (Figure 5, Figure 6, and Figure 7). Such observations agree with the results from DSC analysis, which confirmed the presence of unreacted β-Sn in all 8 h

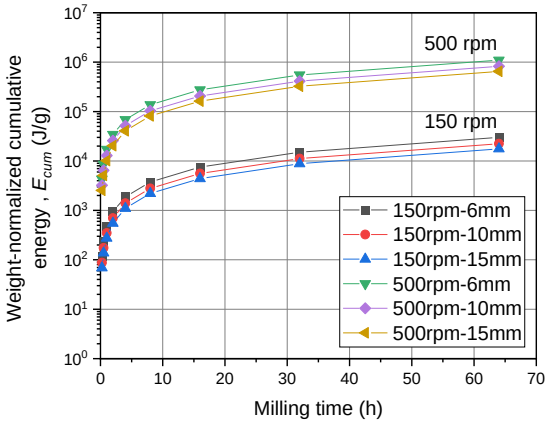

Figure 9 - Calculated weight-normalized cumulative energy transferred to the powders, E_{cum}, as a function of milling time. Based on *Abdellaoui et al.* [22] and *Burgio et al.* [23] models.

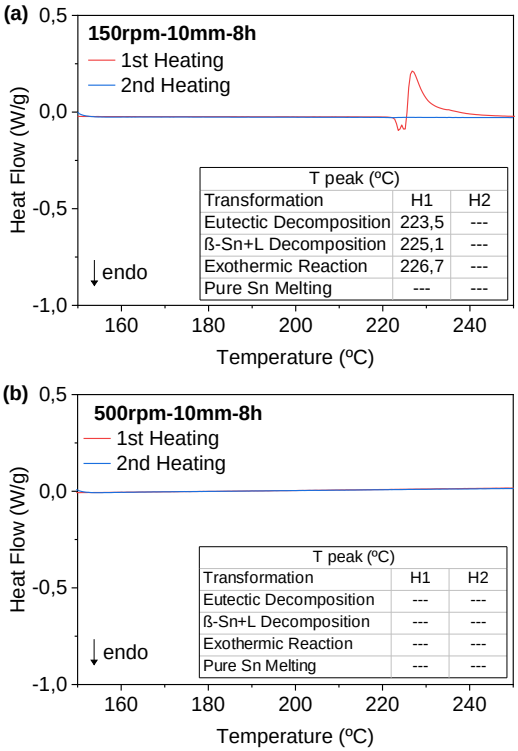

Figure 10 - DSC traces of samples: (a) 150rpm-10mm-8h, and (b) 500rpm-10mm-8h.

samples milled at 150 rpm, whereas for 500 rpm, sample 500rpm-10mm-8h presents no unreacted β-Sn, as can be observed in Figure 10. For 500 rpm, the use of 6 mm and 15 mm balls, particularly 6 mm, was not as efficient since the 8 h milled samples still presented unreacted β-Sn.

In Figure 9, weight-normalized cumulative energy calculations are presented. They show that milling experiments carried out at the same milling rate correspond to two distinct energy regions: 10-10^4 J/g for 150rpm, and 10^3-10^6 J/g for 500 rpm. For a constant milling rate, cumulative energy lies in the same energy region, independently of the milling ball diameter used. Such observations agree with the higher alloying kinetics observed experimentally for higher milling rates, and hence reinforce the governing role of collision power and cumulative energy in determining the reaction kinetics of mechano-synthesis [22,23]. Higher milling rates result in higher frequency of collision, with higher energy values transferred during collision, which increases the reaction kinetics. Powders experience intense mechanical deformation, leading to generation of crystal defects, which together with the balance between cold-welding and fracture events among the powder particles is expected to enhance the microstructural changes of the powder [24]. Also, higher milling rates mean higher peak milling

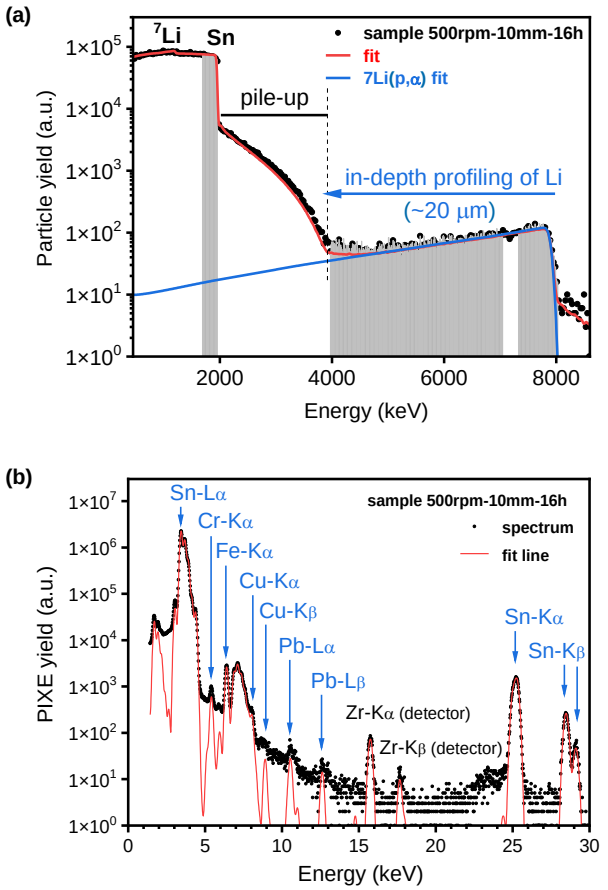

Figure 11 – (a) RBS-NRA integral yield spectra collected from sample 500rpm-10mm-16h, and fit line for elemental analysis. Energy ranges used to map Li and Sn represented as grey windows; (b) PIXE integral yield spectra collected from sample 500rpm-10mm-16h and fit line for elemental analysis.

temperatures at collisions, which increases the reaction kinetics [24].

4.4. Best milling parameters for 50Li-Sn alloy production

Milling experiments at 500 rpm, using 10 mm milling balls, have revealed to be the best to produce the desired equimolar alloy. Upon 2 h milling, a quasi-steady state is achieved, with an almost stationary milling mass yield, $y_M \sim 86\%$, until 64 h of milling, as can be observed in Figure 2. XRD analysis disclosed that, shortly after 2 h milling, a steady state is achieved with all peak intensities (of β-Sn, Li_2Sn_5, and LiSn phases) being similar, with LiSn being the major phase present (Figure 6 and Figure 7). DSC analysis carried out on 500rpm-10mm samples milled for 0.5 h, 2 h, 16 h, 32 h, and 64 h indicated that no remnant β-Sn remained after 0.5 h milling, being all traces similar to the trace of sample 500rpm-10mm-8h, presented in Figure 10b. However, from powder phase composition characterization, no ascertained conclusions could be withdrawn regarding the presence of Li_2Sn_5, or small crystallite size Li-rich Li-Sn intermetallics due to the effect of sample degradation, XRD biased towards the β-Sn phase, and the limited temperature range of DSC analysis.

Additional compositional characterization, through nuclear microprobe analysis (IBA), confirmed that the samples milled for 0.5 h, 2 h, 8 h, and 16 h present elemental homogeneity, with no Sn, nor Li rich zones observed, with Li widely spread in the samples. In Figure 13 are presented the Sn and Li maps obtained for sample 500rpm-10mm-16h. The observed mismatch between Sn-PIXE or Sn-RBS maps, and Li-NRA maps is most likely a result of surface roughness of the pellets, introduced by the press punch, during sample preparation. Although Sn depleted regions (black circles) are observed in Sn-PIXE and Sn-RBS maps, no correspondent Li-rich regions are observed in Li-NRA maps. Preferred orientation, similar to Sn depleted zones, is also observed (dashed arrows). In the case of PIXE, surface roughness leads to partial absorption of emitted Sn-K_α X-rays by surface asperities, which hinders its detection. In the case of RBS, protons backscattered by Sn nuclei located at surface asperities have distinct pathways inside the sample, which results in distinct energy loss before detection [25]. Due to this surface roughness effect, Li maps provided the best information on samples' homogeneity. However, microprobe image pixel size of 3 x 3 μm^2 does not have sufficient resolution to distinguish between the formed Li-Sn intermetallics, LiSn and Li_2Sn_5, with mean crystallite size of ~50 nm (according to Rietveld Refinement results), or even eventual smaller Li-rich Li-Sn intermetallics (according to XRD simulations of Li-rich Li-Sn intermetallics).

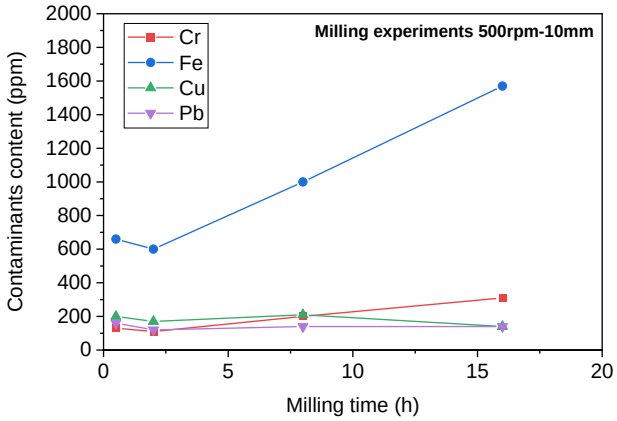

Figure 12 - Contaminants content (ppm) evolution with milling time (h), for the milling experiments 500rpm-10mm determined by μ-PIXE analysis.

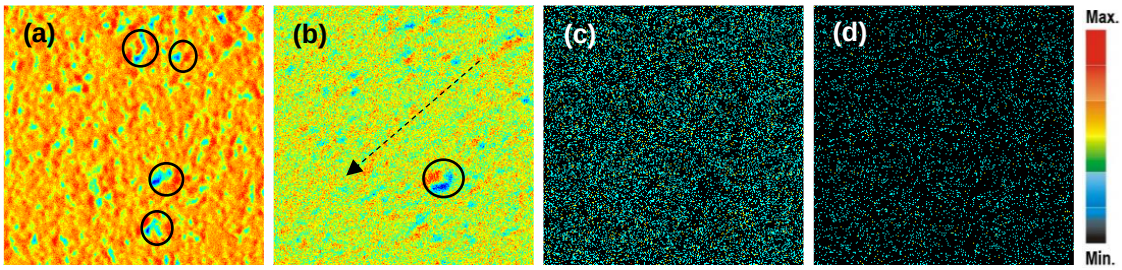

Figure 13 - Sample 500rpm-10mm-16h. 512 x 512 μm^2 maps of (a) Sn-L$_\alpha$ PIXE/ Sn map obtained from Sn-L$_\alpha$ emission in PIXE spectra, (b) Sn-RBS/ Sn map obtained from Sn barrier in RBS, (c) Li bulk NRA/ Li map obtained from Li barrier in NRA, and (d) Li surface NRA/ Li map obtained from Li barrier in NRA. Dashed arrows: direction of the preferred orientation; black circles: Sn depleted regions.

μ-RBS-NRA quantitative elemental analysis of sample milled for 16 h yields an Li excess composition of 58Li-42Sn (at. %). This excess may be attributed to the limitations of the Li cross-sections published for the ^{7}Li(p,α)^{4}He nuclear reaction used for Li quantification [26]. The fit line used for elemental analysis is presented in Figure 11a.

μ-PIXE elemental analysis (Figure 11b) identified the presence of contaminants Cr and Fe, from the milling media; Cu and Pb, from Sn powder, and Zr, from the internal Zr collimator in the detector. Results from PIXE elemental quantification for the four samples are presented in Figure 12. Cu and Pb content do not vary with milling time, remaining below 200 ppm. Contrarily, Fe and Cr content become larger for longer milling times, increasing from 660 ppm and 200 ppm, for 2 h, to 1570 ppm and 310 ppm, for 16 h, respectively.

5. Conclusions

Mechano-synthesis of an equimolar Li-Sn alloy proved to be successful. Overall, all milling experiments present milling mass yields above 40 %, twice as much the values reported for Li-Sn alloys with Li content below 25 at.% (< 20 % [16]). The main source of material loss is powder adhesion and cold-welding to the vial walls with a general increasing tendency with milling time. Adhesion, and cold-welding to the milling balls, accounts for less than 10% of the total mass loss.

XRD and DSC analysis allowed to disclose the reaction path leading to the final targeted alloy microstructure and composition. Mechano-synthesis progresses in two fronts: Li-rich Li-Sn intermetallics preferentially form at the surface of the initial (Li) cuts, whereas Sn-rich Li-Sn intermetallics preferentially form at the surface of the original β-Sn powders. These two fronts converge, at a later stage, to a base LiSn composition, with Li_2Sn_5, and possibly with small crystallite size Li-rich Li-Sn intermetallics. Simulation of XRD diffractograms demonstrated that precise identification of Li-rich Li-Sn intermetallics on XRD diffractograms is a difficult task due to the crystallographic properties of these phases.

Under the experimental conditions used, the results of DRX analysis must be interpreted carefully and complemented with other techniques. The preliminary XRD Context Study allowed to identify vulnerabilities in sample characterization via XRD, when a portable controlled atmosphere sample stage is not available. XRD analysis, supported by complementary DSC analysis, revealed that an induced radiation damage process of the used protective liquid paraffin coating is observed due to X-ray exposure. In addition, complementary GA analysis, allowed the disclosure of XRD bias towards the β-Sn phase and its incapacity to detect the formation of Li-air reaction products during alloy degradation. The later was confirmed by XRD simulation.

As regards to the influence the milling parameters on the final microstructure of the equimolar Li-Sn alloy, both DSC and XRD analysis allowed to conclude that milling rate is the milling parameter presenting the major effect on reaction kinetics. The influence of milling ball diameter is not as pronounced. Weight-normalized cumulative energy calculations, and respective confrontation with the experimental observations, reinforce the governing role of collision power and cumulative energy in determining the reaction kinetics of mechano-synthesis [22,23].

Finally, milling experiments at 500 rpm, using 10 mm milling balls, have revealed to be the best to produce the desired equimolar alloy. Upon 2 h milling, a quasi-steady state is achieved, with an almost stationary milling mass yield, $y_M \sim 86\%$, up to 64 h milling. XRD and DSC analysis identified LiSn has the major phase present, whereas IBA analysis confirmed the elemental homogeneity, with no Sn, nor Li rich zones observed, with Li widely spread in the samples.

References

[1] M.N. Obrovac, V.L. Chevrier, Alloy Negative Electrodes for Li-Ion Batteries, Chem. Rev. 114 (2014) 11444–11502. https://doi.org/10.1021/CR500207G.

[2] R.E. Nygren, F.L. Tabarés, Liquid surfaces for fusion plasma facing components—A critical review. Part I: Physics and PSI, Nucl. Mater. Energy. 9 (2016) 6–21. https://doi.org/10.1016/J.NME.2016.08.008.

[3] Z. Du, Z. Jiang, C. Guo, Thermodynamic optimizing of the Li-Sn system, Int. J. Mater. Res. 97 (2006) 10–16.

[4] F. Taubert, J. Seidel, R. Hüttl, M. Bobnar, R. Gumeniuk, F. Mertens, The heat capacity and entropy of the four lithium stannides Li17Sn4, Li7Sn2, Li13Sn5 and Li7Sn3 in the temperature range (2 to 865) K, J. Chem. Thermodyn. 130 (2019) 119–128. https://doi.org/10.1016/J.JCT.2018.09.035.

[5] T.L. Reichmann, C. Gebert, D.M. Cupid, Investigation of the Li solubility in the intermediate phase Li17Sn4 relevant to understanding lithiation mechanisms in Sn-based anode materials, J. Alloys Compd. 714 (2017) 593–602. https://doi.org/10.1016/J.JALLCOM.2017.04.232.

[6] R.A. Dunlap, D.A. Small, D.D. MacNeil, M.N. Obrovac, J.R. Dahn, Moessbauer effect investigation of the Li-Sn system, J. Alloys Compd. 289 (1999) 135–142. https://doi.org/10.1016/S0925-8388(99)00165-6.

[7] T.L. Reichmann, D. Li, D.M. Cupid, Heat capacities and an updated thermodynamic model for the Li–Sn system, Phys. Chem. Chem. Phys. 20 (2018) 22856–22866. https://doi.org/10.1039/C8CP04205E.

[8] J.P.S. Loureiro, H. Fernandes, F.L. Tabarés, G. Mazzitelli, C. Silva, R. Gomes, E. Alves, R. Mateus, T. Pereira, H. Figueiredo, H. Alves, Deuterium retention in tin (Sn) and lithium–tin (Li–Sn) samples exposed to ISTTOK plasmas, Nucl. Mater. Energy. 12 (2017) 709–713. https://doi.org/10.1016/j.nme.2016.12.026.

[9] Y. Nakajima, M. Kondo, T. Nozawa, Study on fabrication method of lithium alloys with metal grains, Fusion Eng. Des. 98–99 (2015) 2009–2014. https://doi.org/10.1016/j.fusengdes.2015.06.184.

[10] K. Natesan, W.E. Ruther, Fabrication and properties of a tin–lithium alloy, J. Nucl. Mater. 307–311 (2002) 743–748. https://doi.org/10.1016/S0022-3115(02)01221-7.

[11] F.L. Tabarés, E. Oyarzabal, A.B. Martin-Rojo, D. Tafalla, A. de Castro, F. Medina, M.A. Ochando, B. Zurro, K. McCarthy, Experimental tests of LiSn alloys as potential liquid metal for the divertor target in a fusion reactor, Nucl. Mater. Energy. 12 (2017) 1368–1373. https://doi.org/10.1016/J.NME.2016.11.026.

[12] R. Mateus, M.B. Costa, L.C. Alves, N. Catarino, R.C. da Silva, M. Dias, M. Guedes, A.C. Ferro, E. Alves, Ion beam analysis of Li-Sn alloys for fusion applications, in: Nucl. Instruments Methods Phys. Res. Sect. B Beam Interact. with Mater. Atoms, 2021: pp. 55–62. https://doi.org/10.1016/j.nimb.2020.09.019.

[13] R. Mateus, M.B. Costa, L.C. Alves, M. Guedes, E. Alves, A.C. Ferro, Lithium dilution in Li-Sn alloys, Nucl. Mater. Energy. 25 (2020). https://doi.org/10.1016/j.nme.2020.100783.

[14] M.B. Costa, R. Mateus, M. Guedes, A.C. Ferro, Mechanical alloying in the Li-Sn system, Mater. Lett. X. 6 (2020) 100045. https://doi.org/10.1016/j.mlblux.2020.100045.

[15] R. Mateus, M.B. Costa, L.C. Alves, M. Guedes, E. Alves, A.C. Ferro, Hampering deuterium retention in Li-Sn alloys, Nucl. Mater. Energy. (2020) 100783. https://doi.org/10.1016/j.nme.2020.100783.

[16] M.B. Costa, Development of Sn-Li alloys for application in Nuclear Fusion reactors, Instituto Superior Técnico, 2018.

[17] K. Ikeda, S. Terada, T. Mandai, K. Ueno, K. Dokko, M. Watanbe, Lithium-tin Alloy/Sulfur Battery with a Solvate Ionic Liquid Electrolyte, Electrochemistry. 83 (2015) 914–917.

[18] F. Robert, P.E. Lippens, J. Olivier-Fourcade, J.C. Jumas, F. Gillot, M. Morcrette, J.M. Tarascon, Mössbauer spectra as a “fingerprint” in tin-lithium compounds: Applications to Li-ion batteries, J. Solid State Chem. 180 (2007) 339–348. https://doi.org/10.1016/j.jssc.2006.10.026.

[19] F. Robert, P.E. Lippens, R. Fourcade, J.C. Jumas, F. Gillot, M. Morcrette, J.M. Tarascon, Mechanosynthesis and characterisation of the Li-Sn system, Hyperfine Interact. 167 (2006) 797–801. https://doi.org/10.1007/s10751-006-9360-z.

[20] T.B. Massalski, H. Okamoto, P.R. Subramanian, L. Kacprzak, Binary Alloy, Phase Diagrams, 2nd ed., ASM International: Materials Park, OH, 1996.

[21] NIST: X-Ray Mass Attenuation Coefficients - Tin, (n.d.). https://physics.nist.gov/PhysRefData/XrayMassCoef/ElemTab/z50.html (accessed April 26, 2022).

[22] M. Abdellaoui, E. Gaffet, The physics of mechanical alloying in a planetary ball mill: Mathematical treatment, Acta Metall. Mater. 43 (1995) 1087–1098. https://doi.org/10.1016/0956-7151(95)92625-7.

[23] N. Burgio, A. Iasonna, M. Magini, S. Martelli, F. Padella, Mechanical alloying of the Fe-Zr system. Correlation between input energy and end products, Nuovo Cim. 13 (1991) 459–476. https://doi.org/10.1007/BF02452130.

[24] C. Suryanarayana, Mechanical alloying and milling, Mech. Alloy. Milling. 46 (2004) 1–472. https://doi.org/10.4150/kpmi.2006.13.5.371.

[25] S.L. Molodtsov, A.F. Gurbich, C. Jeynes, Accurate ion beam analysis in the presence of surface roughness, J. Phys. D. Appl. Phys. 41 (2008) 1–7. https://doi.org/10.1088/0022-3727/41/20/205303.

[26] J.W. Mayer, E. Rimini, Ion Beam Handbook for Material Analysis, Academic Press, London, UK, 1977.